ECCOMAS Congress 2016
VII European Congress on Computational Methods in Applied Sciences and Engineering
M. Papadrakakis, V. Papadopoulos, G. Stefanou, V. Plevris (eds.)
Crete Island, Greece, 5–10 June 2016

NUMERICAL ANALYSIS OF RADIO FREQUENCY BLACKOUT FOR ATMOSPHERIC REENTRY VEHICLE USING CFD-CEM COMBINED METHOD

Yusuke Takahashi[1], Reo Nakasato[2], and Nobuyuki Oshima[3]

[1]Hokkaido University
Kita 13 Nishi 8, Kita-ku, Sapporo, Hokkaido, 060-8628 Japan
e-mail: ytakahashi@eng.hokudai.ac.jp
and
[2]Hokkaido University
Kita 13 Nishi 8, Kita-ku, Sapporo, Hokkaido, 060-8628 Japan
e-mail: reopon717@eis.hokudai.ac.jp
and
[3]Hokkaido University
Kita 13 Nishi 8, Kita-ku, Sapporo, Hokkaido, 060-8628 Japan
e-mail: oshima@eng.hokudai.ac.jp

Keywords: Radio Frequency Blackout, Atmospheric Reentry Capsule, Hypersonic Flow Solver, FD2TD Method

Abstract. *Numerical simulations of electromagnetic waves around the atmospheric reentry demonstrator (ARD) of the European Space Agency (ESA) in an atmospheric reentry mission were conducted with a combined method of computational fluid dynamics (CFD) and computational electromagnetics (CEM). During the reentry mission, radio frequency blackout and plasma attenuation of radio waves in communications with a data-relay satellite were observed. Cut-off of waves propagation was caused by highly dense plasma formed by a strong shock wave formed in front of the vehicle due to orbital speed. In this study, the physical properties of the plasma flow in the shock layer and wake region of the ESA ARD were obtained using a high-enthalpy flow solver applicable unstructured grids. Moreover, electromagnetic waves were calculated using a frequency-dependent finite-difference time-domain method using the plasma properties. The present analysis model was validated based on experimental flight data of ESA ARD. Comparisons of the measured and predicted results showed good agreements. Attenuation and reflection by reentry plasma were clarified in detail using the present model. It was suggested that the analysis model could be an effective tool for investigating radio frequency blackout and plasma attenuation in radio wave communication. Behaviors of plasma and electromagnetic waves around ESA ARD for several altitudes were investigated using the proposed model in detail.*

1 INTRODUCTION

One of the most important issues in the entry, descent, and landing approach of spacecraft is radio frequency (RF) blackout; that is, the cutoff of communication between the reentry vehicle and ground stations and/or data-relay satellites. During reentry from a low Earth orbit, a vehicle flies at orbital speed of more than 7 km/s, and a strong shock wave is formed at its front. Freestream air is rapidly dissociated by aerodynamic heating in the shock wave layer. Charged species, i.e., electrons and ions, are created, and these species then cover the vehicle's surface. RF blackout is caused by a highly dense plasma layer on the vehicle surface, attenuating or reflecting electromagnetic waves used for telecommunication.

Because the RF blackout phenomenon is affected by the flow properties around the vehicle, specifically the number density of electrons, clarifying the distribution of charged particles is a key issue. In particular, determination of the plasma distribution around a blunt-body reentry capsule is expected to be important from the point of view of their frequent use in reentry missions. Recently, remarkable progress has been made in the development of high-performance computers and algorithms for numerical simulation. Computational fluid dynamics (CFD) techniques have been used widely to predict flow fields around reentry vehicles. In addition, computational electromagnetics (CEM) to describe electromagnetic waves in reentry plasma are also important approach. In particular, the frequency-dependent finite-difference time-domain (FD2TD) method [1] has also been an effective tool for simulating electromagnetic waves in a frequency-dependent medium [2]. An analysis approach to predict RF blackout and plasma attenuation for a reentry vehicle, based on a method combining CFD and CEM, has been suggested by Takahashi et al. [3, 4, 5].

Flight experiment for the atmospheric reentry demonstrator (ARD) [6] of the European Space Agency (ESA) was conducted. In the ESA ARD mission, reentry plasma attenuation of electromagnetic waves in communication with the tracking and data-relay satellite (TDRS) was measured. ESA ARD had typical blunt-body capsule shape and typical reentry trajectory, which are widely used in a reentry mission. Thus, it is worth investigating the distributions of plasma and electromagnetic waves for design and development of new reentry vehicles and for research and development concerning RF blackout mitigation techniques. Takahashi [5] recently developed an RF blackout prediction tool combining RG-FaSTAR, which is a high-enthalpy flow solver applicable to unstructured grid systems, and FD2TD simulation code. Using the analysis models, it is possible to investigate the behavior of electromagnetic waves in reentry plasma. The present research objective is to reproduce the actual reentry environment during the ESA ARD flight and to clarify the plasma flow field and electromagnetic wave behavior.

2 ATMOSPHERIC REENTRY DEMONSTRATOR

The atmospheric reentry demonstrator (ARD) [6] of the European Space Agency (ESA) was launched by the Ariane-5 V503 rocket on October 21, 1998. The reentry capsule was separated from the Ariane-5 at an altitude of 218 km. ESA ARD reached its apogee at an altitude 830 km, and then reentered the Earth's atmosphere. It was reported that the reentry velocity at an altitude of 120 km was approximately 7452 m/s. Because of its high reentry velocity, a shock wave was generated in front of the vehicle, and the vehicle was surrounded by plasma. After deceleration by the aerodynamic force, ESA ARD began its recovery sequence. Finally, ESA ARD splashed down in the Pacific Ocean. The reentry trajectory (position, velocity, and attitude reconstructed by acceleration measurements) was obtained using on-board inertial navigation system measurements and a GPS receiver.

The analytical shape of the ESA ARD is shown in Fig. 1. Its shape was basically the same as the Apollo command module scaled down to 70%. It comprised the front shield section, rear cone section, and back cover section. The capsule was essentially a spherical cone with a nose radius of 3,360 mm and a base radius of 2,800 mm for the front shield section with a half-angle of 33° for the rear section. To protect it from strong aerodynamic heating, an ablator material was coated onto the front heat shield.

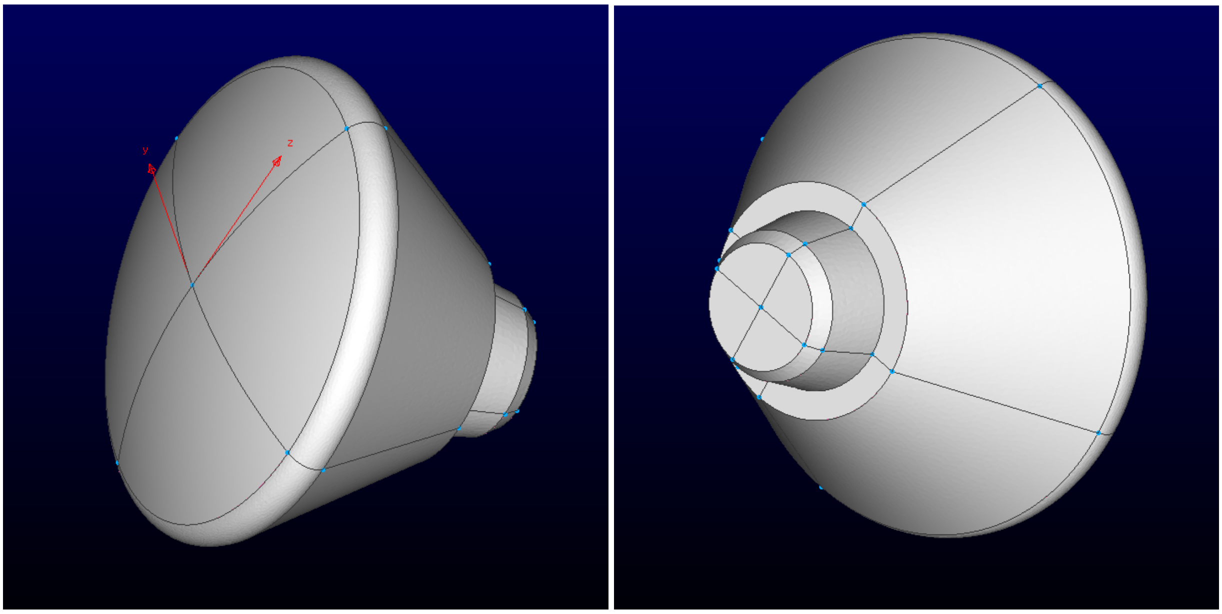

(a) Front side view (b) Rear side view

Figure 1: Analysis model of the ESA ARD.

ESA ARD employed eight dedicated skin antennas for a telemetry link and communication with TDRS. Its link frequencies were approximately 2.267 GHz. Measurements were made of the RF blackout and plasma attenuation caused by the plasma around the vehicle generated by the shock wave. No RF blackout for the TDRS link was observed, even though strong plasma attenuation due to reentry plasma around ESA ARD was measured from an altitude of 86 km to an altitude of 44 km.

3 PLASMA FLOW MODELING

Physical model and numerical method used in this plasma flow simulation are basically the same as those used in Takahashi's work [5], except for part numerical scheme and calculation conditions. Here, brief explanation about the present plasma flow model are presented.

3.1 ANALYSIS MODEL

The flow field around the reentry capsule is expressed by the Navier-Stokes equations extended to a multi-temperature model and the equation of state. The governing equations include total mass, momentum, total energy, species mass, rotation energy, vibration energy, and electron energy conservations.

Transport properties such as the viscosity, thermal conductivity, and binary diffusion coefficients for a gas mixture are evaluated by Yos's model [7], which is based on the first Chapman-Enskog approximation [8]. The collision cross sections are given by Gupta [9] and Fertig

[10, 11]. The diffusion coefficients are expressed by Curtiss and Hirschfelder's formula [12]. Ambipolar diffusion is assumed for charged species.

For chemical reactions, the inflow gas is assumed to consist of 11 chemical species ($\mathrm{N_2}$, $\mathrm{O_2}$, NO, $\mathrm{N_2^+}$, $\mathrm{O_2^+}$, $\mathrm{NO^+}$, N, O, $\mathrm{N^+}$, $\mathrm{O^+}$ and $\mathrm{e^-}$) and 49 reactions are assumed to occur. The chemical reaction rate is determined using an Arrhenius-type form, and the reaction rate coefficients are obtained from Park [13]. The backward reaction rates are evaluated from the equilibrium constants which, being functions of temperature only, are calculated by the curve-fitting formula given in [14, 9].

The energy transfer between each of the internal energy modes are consider as follows: translation-rotation (T-R) [15], translation-vibration (T-V) [16, 17], translation-electron (T-e) [18, 19, 20], rotation-vibration (R-V) [21], rotation-electron (R-e) [22, 23], and vibration-electron (V-e) [24]. The energy losses/releases for vibrations and rotations associated with chemical reactions reveal the dissociation energies for heavy-particle impact reactions. These can be obtained using a non-preferential dissociation model [20]. In addition, the electron energy losses/releases due to electron-impact dissociation and ionization are also considered.

3.2 NUMERICAL SCHEMES

The governing equations for the flow field are transformed into the delta form and solved using a finite-volume approach. The numerical fluxes of the advection term are calculated using the Harten, Lax, van Leer, and Einfeldt (HLLE) scheme [25] using the monotonic upstream-centered scheme for interpolation of the conservation laws (MUSCL). On the other hand, the viscous terms of the equation are calculated using the second-order central differencing method. The spatial gradients of the flow variables are evaluated with the Green-Gauss method. A time integration is performed implicitly using the lower-upper symmetric Gauss-Seidel (LU-SGS) method [26] combined with the point-implicit method [27] for stable computation.

3.3 SOFTWARE PACKAGE

These physical and numerical models are implemented in the high-enthalpy flow solver RG-FaSTAR [5]. RG-FaSTAR is a version of the fast unstructured CFD code FaSTAR [28] originally developed by JAXA that incorporates real gas effects. These solvers can handle unstructured grid systems such as tetrahedral, triangular prism, square pyramid, and hexahedral meshes, and have high flexibility in generating the computational grid. For massive parallel computation on high-performance computers, the message-passing interface (MPI) technique with a domain partition approach is used.

3.4 CALCULATION CONDITIONS

Numerical analyses of flow fields by RG-FaSTAR are performed for cases as listed in Table 1. Note that AOA denotes the angle of attack of the ESA ARD. The freestream velocity is determined according to Tran's report [6].

Computational grids for ESA ARD in RG-FaSTAR at an altitude of 85 km are composed of tetrahedral meshes, prismatic layer meshes near the wall, hexahedral meshes in the front region, and squared pyramids. Figure 2 shows a computational grids at an altitude of 85 km. To finely resolve the shock layer near ESA ARD, hexahedral meshes are inserted into its front region. In addition, prismatic meshes near walls are used to solve the boundary layer near the wall. Square pyramid meshes are used to connect the hexahedral meshes and the prism meshes. The numbers of cells and nodes of the grid system at altitude of 85 km are 4,244,601 and 2,434,920,

Table 1: Freestream parameters.

Altitude, km	Density, kg/m^3	Temperature, K	Velocity, m/s	AOA, degree
85.0	8.18×10^{-6}	191.0	7577	20.0
80.0	1.85×10^{-5}	195.8	7609	20.0
75.0	4.07×10^{-5}	201.7	7593	19.2
70.0	8.83×10^{-5}	210.9	7542	19.2
65.0	1.78×10^{-4}	225.3	7145	20.0
60.0	3.40×10^{-4}	256.5	6105	19.4
55.0	6.31×10^{-4}	242.0	5393	19.8
50.0	1.15×10^{-3}	265.3	4567	20.0
45.0	2.25×10^{-3}	255.6	3323	20.8
40.0	4.36×10^{-3}	250.3	2218	21.2

respectively. At other altitudes, the number of cells and nodes are different but the composition of mesh types is basically similar.

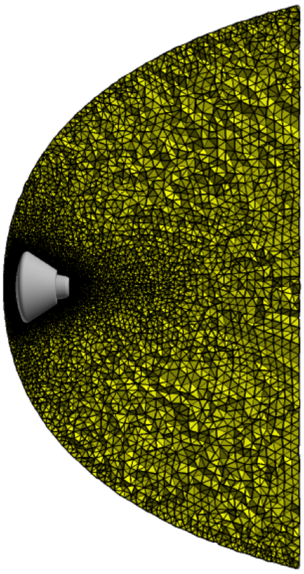

Figure 2: Computational grids system for plasma flow around ESA ARD at altitude of 85 km.

For the boundary conditions, inlet, outlet, and wall conditions are considered, as shown in Fig. 3. Freestream density, temperature, and velocity, listed in Table 1, are given at the inflow boundary. Mass fractions of chemical species are always set to 0.765 for N_2 and 0.235 for O_2 at the inflow. The degree of ionization at the inflow condition is always set to 10^{-10}. At the outlet boundary, all flow variables are determined by the zeroth-order extrapolation. On the wall surface, non-pressure gradient in the wall normal direction and no-slip wall are given. In addition, the wall temperature is fixed at 273K. Moreover, the wall surface is assumed to be non catalytic for chemical species.

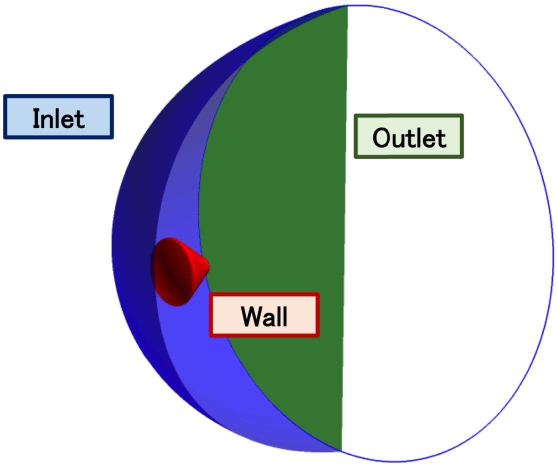

Figure 3: Boundary conditions for plasma flow around ESA ARD at altitude of 85 km.

4 ELECTROMAGNETIC WAVE MODELING

4.1 GOVERNING EQUATION

In order to evaluate RF blackout and plasma attenuation in communication between ESA ARD and TDRS, we clarify the behavior of electromagnetic waves in the plasma region during reentry. Here, the Maxwell's equations for describing the behavior of electromagnetic waves are adopted.

4.2 COMPUTATION METHOD

So far, the finite-difference time-domain (FDTD) method has been widely used for simulating electromagnetic wave propagation. On the other hand, plasmas are generally frequency-dependent media. Dielectric constants and electrical conductivities of plasma vary over a frequency range. It is possible that the FDTD formulation leads to a risk to predict incorrect results when applying it to frequency-dependent media, because the FDTD method assumes that these medium properties are independent of frequency. On the other hand, the FD2TD method is effective for discretizing the Maxwell's equations in such frequency-dependent media.

Figure 4 shows the computational domain in the FD2TD approach for cases of altitudes from 55 to 40 km. it should be noted that different computational domains are used at the other altitudes. The computational domain for electromagnetic waves is set to be a cuboid 10.5 m in length in the x direction, 5.5 m in width in the y direction, and 5.0 m in height in the z direction. All of the computational grid is composed of hexahedral meshes and the grid nodes are set to 800 (x-direction), 420 (y-direction), and 380 (z-direction), i.e., 127,680,000 nodes. The origin of the computational domain used in the CFD approach corresponds to that of the simulation of the electromagnetic waves. The physical properties, ω_{p} and ν_{c}, required in the present FD2TD method are obtained by using the computational results obtained by RG-FaSTAR. To reduce computational cost, the magnetic permeability, μ is set to be the same as that of free space, μ_0.

As a boundary condition, Mur's first-order absorption boundary [29] is imposed at all faces of the computational domain. A conduction boundary condition is imposed on the surface of the reentry vehicle.

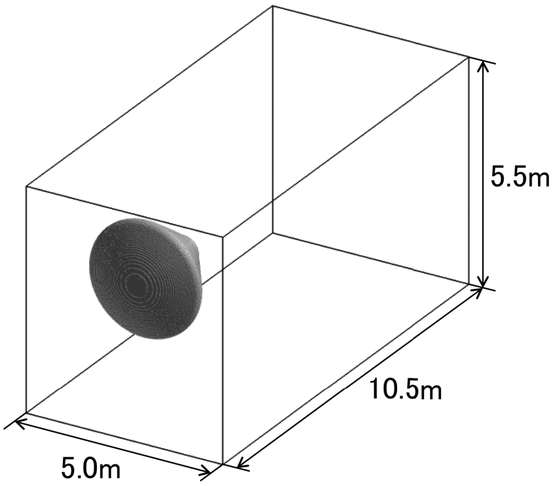

Figure 4: Computational domain for electromagnetic wave around ARD.

4.3 ANALYSIS CODE

The physical and numerical models have been implemented in the electromagnetic wave simulation code “Arcflow/Arcwave” developed by Hokkaido University. For fast computation and efficient allocation of adequate memory, the simulation code is parallelized using the MPI and OpenMP techniques. In addition, a data transfer tool between the electromagnetic wave simulation code and RG-FaSTAR is also implemented. Both the simulation codes using the CFD and FD2TD methods are packaged.

5 RESULTS AND DISCUSSION

5.1 SURFACE PRESSURE

First of all, to validate the plasma flow analysis model used here, stagnation pressure coefficients in front of the ESA ARD between the flight experiment and numerical analysis are compared. The pressure obtained in the ESA ARD flight was reconstructed based on the flight data on velocity and density deduced by the on-board acceleration measurement. The computed pressure coefficient at stagnation, C_p, is defined as the peak pressure on the front surface of the vehicle, which is obtained by the following expression:

$$C_p = \frac{p_0}{\frac{1}{2}\rho_\infty U_\infty^2}, \tag{1}$$

where p_0 is the peak pressure on the surface. In addition, ρ_∞ and U_∞ are the freestream density and velocity, respectively. Figure 5 shows a comparison of the stagnation pressure coefficient profiles with altitude from 85 km to 40 km. Error between the flight experiment results and the numerical analysis is several percentages at most except for an altitude of 85 km. This indicates that the plasma flow analysis correctly reproduces the aerodynamic tendencies in the shock layer.

5.2 SIGNAL LOSS

Gain of the electromagnetic waves is attenuated by plasma around the reentry vehicle, which was measured in the ESA ARD mission. To validate the CFD and CEM combined method,

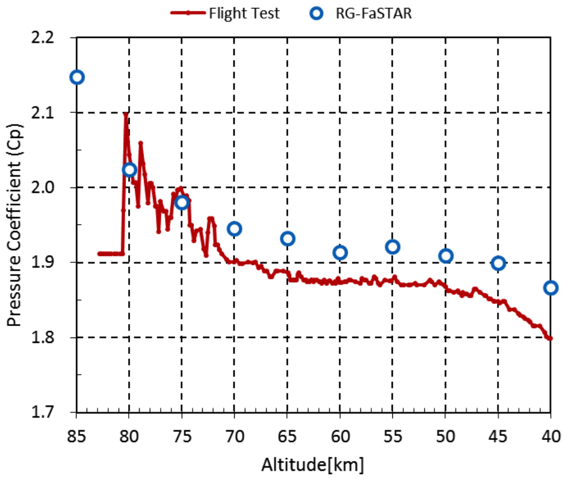

Figure 5: Comparison of the pressure coefficient at stagnation at the vehicle's front between the flight experiment and numerical analysis.

signal loss of the electromagnetic waves that TDRS received are compared between the experiments by ESA ARD mission and the present computed results. When the vehicle is completely surrounded by highly dense plasma whose electron number density exceeds the critical value, no signal is detected, and then RF blackout is observed. In the present study, the signal loss is calculated by

$$G_{\mathrm{SL}} = -10\log\left(\frac{|\mathbf{E}_{bd}|^2}{|\mathbf{E}_{bd,free}|^2}\right). \tag{2}$$

where $\mathbf{E}_{bd}$ and $\mathbf{E}_{bd,free}$ are the electric fields on certain far field boundary at an altitude and in free space where there is no plasma, respectively. The location of the TDRS from the viewpoint of ESA ARD during reentry can be obtained from its flight path. In addition, it is deduced that the windows where the TDRS is visible at each altitude shown in Fig. 6 are on the boundaries of the FD2TD computational domain.

Comparison of the signal loss profile along an altitude is shown in Fig. 7. The measured attenuation of the communication waves increases with small fluctuation to altitude of 70 km, and then, the communication recovers with decrease in attenuation. No RF blackout is observed in the flight experiment as an important event. The computed result relatively shows good agreement with the measurement at altitude of 85 km and below 60 km. However, at altitudes between 80 km and 65 km, electromagnetic waves near ESA ARD are completely blocked by the reentry plasma, and then the signal loss almost becomes zero. This is possibly because the plasma flow simulation overestimates number density of electron in the rear region of ESA ARD. In particular, reaction models of associative ionizations which are primary ionization and recombination reactions of electrons in the altitude range can attribute the discrepancy.

5.3 ELECTRON NUMBER DENSITY

The distribution of electron number density around ESA ARD at an altitude of 85 km is shown in Fig. 8. In these figures, "y-z plane" shows a plane cutting a region where antenna for communication with TDRS exists. A region appears to exist in which the electron number density generated by the shock layer in front of ESA ARD remains high at the altitude. When the electromagnetic waves pass through the regions where the electron density exceeds the

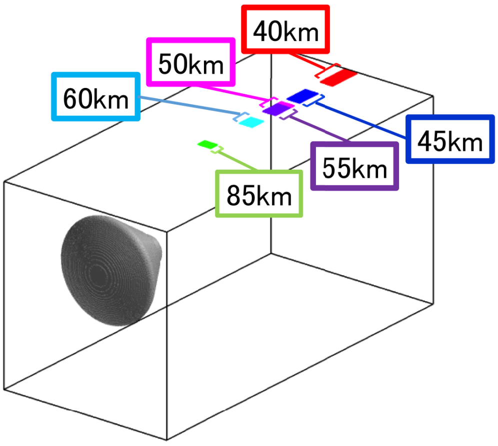

Figure 6: Windows in which the TDRS is visible at each altitude on the boundaries of the FD2TD domain.

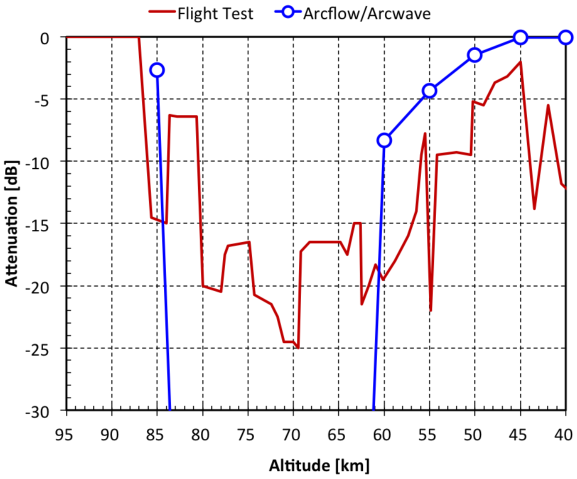

Figure 7: Comparison of the signal loss between the flight experiment and numerical analysis.

critical value (6.4×10^{16} 1/m^3) for the link frequency (2.267 GHz), attenuation, refraction, or reflection will occur. On the other hand, compressed gas in the shock layer expands when passing near the shoulder of the vehicle inflowing in the wake region. The plasma density decreases to well below the critical value at the rear of the vehicle because of its supersonic expansion.

5.4 ELECTROMAGNETIC WAVES

Number density of electron and collision frequency required in the electromagnetic wave calculations are computed by RG-FaSTAR and then, are transposed in the FD2TD computational domain with the data transfer tool. Figures 9, 10, 11, and 12 show electric field magnitudes of the electromagnetic waves for the cases of free space, an altitude of 85 km, an altitude of 60 km, and an altitude of 50 km, respectively. The magnitude of the electric field is normalized to 1.0 on the antenna in the calculation. All values of the electric field in the figures are expressed on a logarithmic scale.

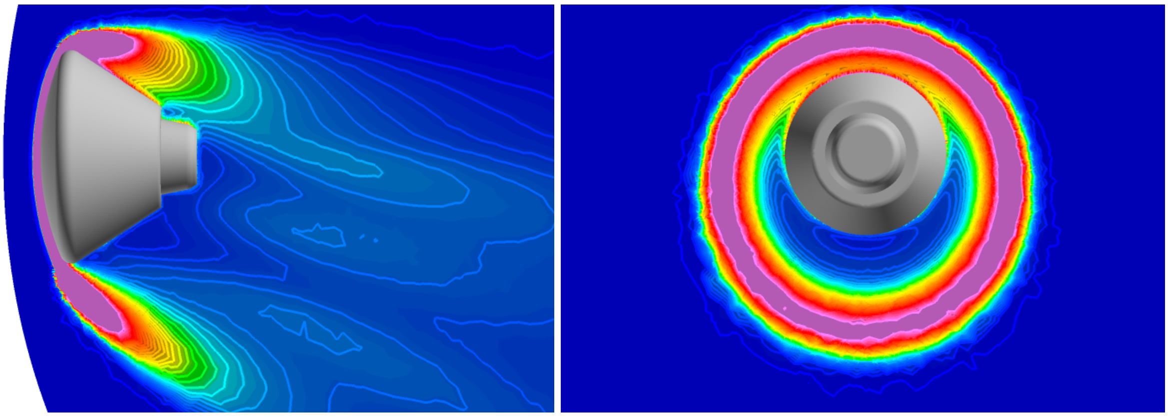

(a) x-z plane (b) y-z plane

Figure 8: Number density of electrons around the ESA ARD at an altitude of 85 km.

The electric field distribution in free space where there is no plasma is presented to compare with results for cases of other altitudes. For the free-space condition, the electromagnetic waves can propagate in all directions, diffracting and reflecting on the ESA ARD surface. On the other hand, below an altitude of 85 km, electromagnetic waves cannot propagate on the front side of ESA ARD along the shock layer surface, because electromagnetic waves are completely reflected. As mentioned above, moreover, electromagnetic waves cannot propagate in any direction between altitudes of 80 km and 65 km due to highly-dense plasma. Thus, a complete RF blackout occurs, although this is not shown here. As mentioned above, however, this RF blackout was not observed in communication between ESA ARD and the TDRS using a link frequency of 2.267 GHz during atmospheric reentry. Uncertainties in chemical reaction models used in this analysis model causes this discrepancy, as pointed out by Takahashi et al. [4]. At an altitude of 60 km, wave propagation recovers from the RF blackout, while strong attenuation and reflection in the plasma wake are caused by the recompression gas region. The number density of electrons becomes low in the ESA ARD's rear region at an altitude of 50 km and electromagnetic waves propagate in a similar fashion to the computed results for the free-space condition.

6 CONCLUSIONS

Numerical analyses of plasma flows and communication waves around the Atmospheric Reentry Demonstrator (ARD) were conducted for prediction of radio frequency blackout and plasma attenuation. The ESA ARD capsule shape and its reentry trajectory were typical for reentry missions with blunt-body reentry capsules. The plasma flow models were implemented with an unstructured grid high-enthalpy flow solver "RG-FaSTAR" based on the computational fluid dynamics (CFD). Moreover, electromagnetic waves behaviors were expressed using a simulation code "Arcflow/Arcwave," which uses the frequency-dependent finite-difference time-domain (FD2TD) method. Computed results were validated with experimental data for stagnation pressure and signal loss profiles during the atmospheric reentry. It was indicated that the present analysis model is effective for predicting reentry plasma and signal loss of radio waves for this kind of reentry capsule mission, except for a strong attenuation altitude. As an important parameter for electromagnetic wave simulation in reentry plasma, distributions of the electron number density were investigated. In addition, radio frequency blackout and plasma attenuation were discussed using information. It was found that reflection, diffraction, and attenuation on

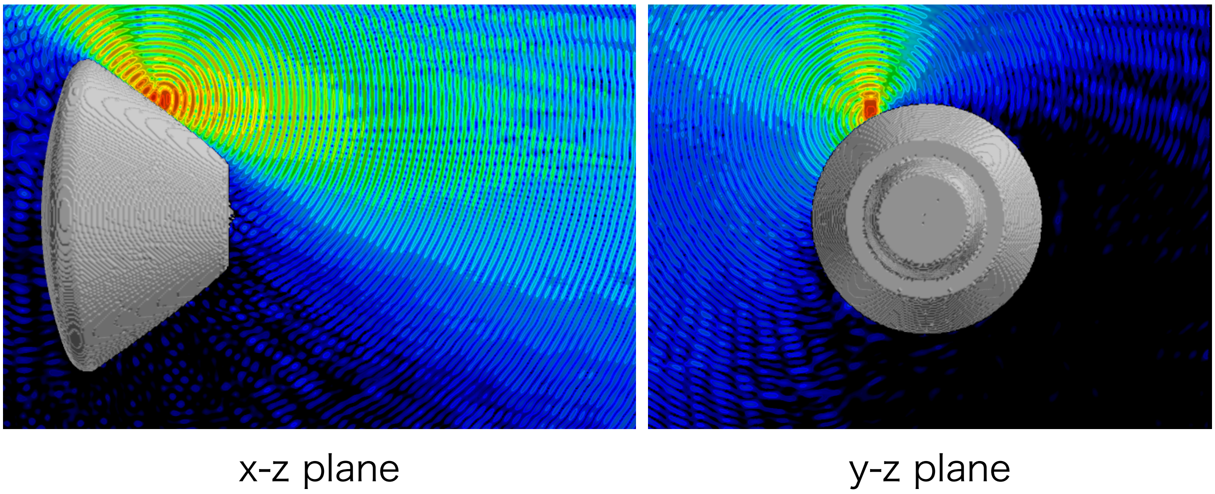

Figure 9: Electromagnetic waves behavior (electric field magnitude in common logarithm scale) around ESA ARD in free space.

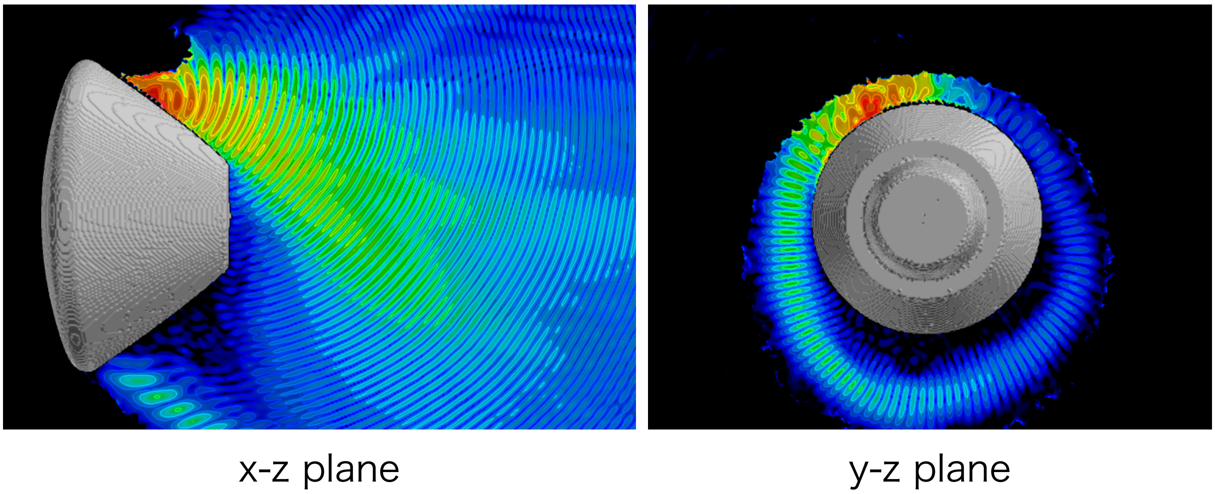

Figure 10: Electromagnetic waves behavior (electric field magnitude in common logarithm scale) around ESA ARD at an altitude of 85 km.

the strong shock wave surface in front of the vehicle occur, while the electromagnetic waves propagate in wake region in the rear of vehicle.

Acknowledgments

This work was supported by JSPS KAKENHI Grant Number 26820366. The present computational results were obtained using the fast unstructured CFD code "FaSTAR," which was developed by the Japan Aerospace Exploration Agency (JAXA). This research used computational resources of the HPCI system provided by the Information Initiative Center, Hokkaido University through the HPCI System Research Project (Project ID:hp150100). The computations were performed mainly using the computational facilities (HITACHI HA8000-tc/HT210 and HITACHI SR16000 VM1) at the Research Institute for Information Technology, Kyushu University, and the supercomputer system (HITACHI SR16000 model M1) at the Information

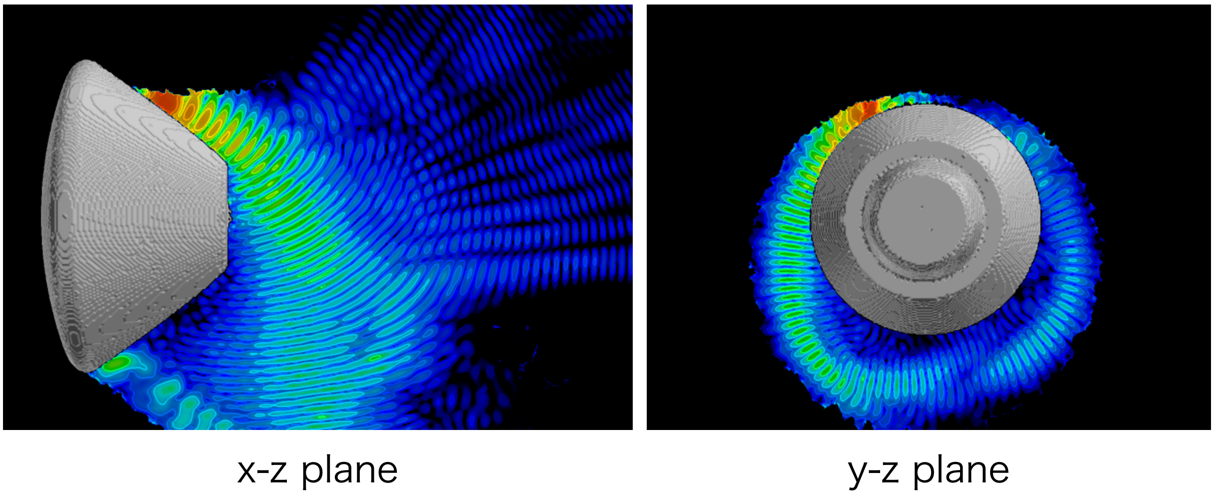

Figure 11: Electromagnetic waves behavior (electric field magnitude in common logarithm scale) around ESA ARD at an altitude of 60 km.

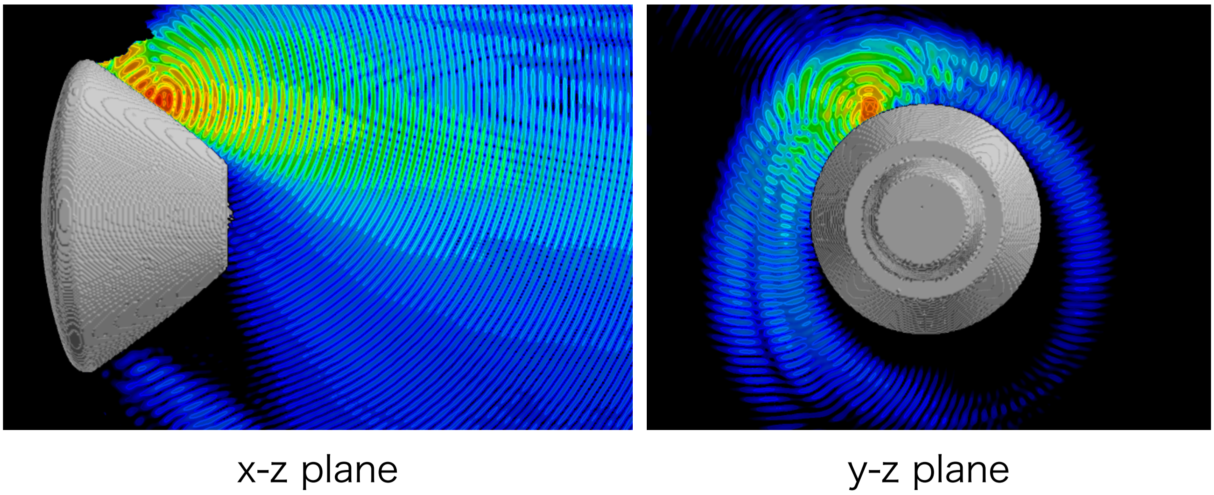

Figure 12: Electromagnetic waves behavior (electric field magnitude in common logarithm scale) around ESA ARD at an altitude of 50 km.

Initiative Center, Hokkaido University.

REFERENCES

[1] K.S. Kunz and R.J. Luebbers. *The Finite Difference Time Domain Method for Electromagnetics*. CRC Press, Boca Raton, 1993.

[2] K. Kinefuchi, I. Funaki, and T. Abe. “Frequency-Dependent FDTD Simulation of the Interaction of Microwaves With Rocket-Plume”. *IEEE Transactions on Antennas and Propagation*, 58(10):3282–3288, October 2010.

[3] Y. Takahashi, K. Yamada, and T. Abe. “Examination of Radio Frequency Blackout for an Inflatable Vehicle during Atmospheric Reentry”. *Journal of Spacecraft and Rockets*, 51(2):430–441, March 2014.

[4] Y. Takahashi, K. Yamada, and T. Abe. “Prediction Performance of Blackout and Plasma Attenuation in Atmospheric Reentry Demonstrator Mission”. *Journal of Spacecraft and Rockets*, 51(6):1954–1964, Novermber 2014.

[5] Y. Takahashi. “Advanced validation of CFD-FDTD combined method using highly applicable solver for reentry blackout prediction”. *Journal of Physics D: Applied Physics*, 49(1):015201, 2016.

[6] P. Tran, J.C. Paulat, and P. Boukhobza. “Re-entry Flight Experiments Lessons Learned - The Atmospheric Reentry Demonstrator ARD”. *Nato Report, RTO-EN-AVT-130-10*, pages 10–1 – 10–46, June 2007.

[7] J.M. Yos. “Transport Properties of Nitrogen, Hydrogen Oxygen and Air to 30,000 K”. *TRAD-TM-63-7,* Research and Advanced Development Division, AVCO Corp., 1963.

[8] J.O. Hirschfelder, C.F. Curtiss, and R.B. Bird. *Molecular Theory of Gases and Liquids*. Wiley, New York, 1954.

[9] R.N. Gupta, J.M. Yos, R.A. Thompson, and K.P. Lee. “A Review of Reaction Rates and Thermodynamic and Transport Properties for an 11-Species Air Model for Chemical and Thermal Nonequilibrium Calculations to 30000 K”. *NASA RP-1232*, Aug. 1990.

[10] M. Fertig, A. Dohr, and H.H. Frühaufu. “Transport Coefficients for High-Temperature Nonequilibrium Air Flows”. *AIAA Paper 98-2937*, 1998.

[11] M. Fertig, A. Dohr, and H.H. Frühauf. “Transport Coefficients for High-Temperature Nonequilibrium Air Flows”. *Journal of Thermophysics and Heat Transfer*, 15(2):148–156, April-June 2001.

[12] C.F. Curtiss and J.O. Hirschfelder. “Transport Properties of Multicomponent Gas Mixture”. *Journal of Chemical Physics*, 17(6):550–555, June 1949.

[13] C. Park. “Assessment of a Two-Temperature Kinetic Model for Dissociating and Weakly Ionizing Nitrogen”. *Journal of Thermophysics and Heat Transfer*, 2(1):8–16, Jan.-March 1988.

[14] C. Park. *Nonequilibrium Hypersonic Aerothermodynamics*. Wiley, New York, 1990.

[15] J.G. Parker. “Rotational and Vibrational Relaxation in Diatomic Gases”. *The Physics of Fluids*, 2(4):449–462, July-Aug. 1959.

[16] R.C. Millikan and D.R. White. “Systematics of Vibrational Relaxation”. *The Journal of Chemical Physics*, 39(12):3209–3213, Dec. 1963.

[17] C. Park. “Problems of Rate Chemistry in the Flight Regimes of Aeroassisted Orbital Transfer Vehicles”. *AIAA Paper 84-1730*, 1984.

[18] J.P. Appleton and K.N.C. Bray. “The Conservation Equations for a Nonequilibrium Plasma”. *Journal of Fluid Mechanics*, 20(4):659–672, June 1964.

[19] M. Mitchner and C.H. Kruger Jr. *Partially Ionized Gases*. Wiley, New York, 1973.

[20] P.A. Gnoffo, R.N. Gupta, and J.L. Shinn. "Conservation Equations and Physical Models for Hypersonic Air Flows in Thermal and Chemical Nonequilibrium". *NASA TP-2867*, Feb. 1989.

[21] C. Park. "Rotational Relaxation of N_2 Behind a Strong Shock Wave". *Journal of Thermophysics and Heat Transfer*, 18(4):527–533, Oct.-Dec. 2004.

[22] M. Nishida and M. Matsumoto. "Thermochemical Nonequilibrium in Rapidly Expanding Flows of High-Temperature Air". *Zeitschrift für Naturforschung, Teil A: Physik, Physikalische Chemie, Kosmophysik*, 52(4):358–368, 1997.

[23] S.S. Lazdinis and S.L. Petrie. "Free Electron and Vibrational Temperature Nonequilibrium in High Temperature Nitrogen". *Physics of Fluids*, 17(8):1539–1546, Aug. 1974.

[24] J.H. Lee. "Electron-Impact Vibrational Relaxation in High-Temperature Nitrogen". *Journal of Thermophysics and Heat Transfer*, 7(3):399–405, July-Sept. 1993.

[25] B. Einfeldt. "On Godunov-type methods for gas dynamics". *SIAM Journal on Numerical Analysis*, 25(2):294–318, 1988.

[26] A. Jameson and S. Yoon. "Lower-Upper Implicit Schemes with Multiple Grids for the Euler Equations". *AIAA Journal*, 25(7):929–935, July 1987.

[27] T.R.A. Bussing and E.M. Murman. "Finite-Volume Method for the Calculation of Compressible Chemically Reacting Flows". *AIAA Journal*, 26(9):1070–1078, 1988.

[28] A. Hashimoto, K. Murakami, T. Aoyama, K. Ishiko, M. Hishida, M. Sakashita, and P.R. Lahur. "Toward the Fastest Unstructured CFD". *AIAA Paper 2012-1075*, 2012.

[29] G. Mur. "Absorbing Boundary Conditions for the Finite-Difference Approximation of the Time-Domain Electromagnetic-Field Equations". *IEEE Transactions on Electromagnetic Compatibility*, EMC-23(4):377–382, 1981.